ADVANCED FUNCTIONAL MATERIALS

Postfach 10 11 61
69451 Weinheim
Germany
Courier services:
Boschstraße 12
69469 Weinheim
Germany
Tel.: (+49) 6201 606 531
Fax: (+49) 6201 606 500
E-mail: afm@wiley.com

WILEY-VCH

Dear Author,

Please correct your galley proofs carefully and return them no more than four days after the page proofs have been received.

Please limit corrections to errors already in the text; cost incurred for any further changes or additions will be charged to the author, unless such changes have been agreed upon by the editor.

The editors reserve the right to publish your article without your corrections if the proofs do not arrive in time.

Note that the author is liable for damages arising from incorrect statements, including misprints.

Please note any queries that require your attention. These are indicated with a Q in the PDF and a question at the end of the document.

Reprints may be ordered by filling out the accompanying form.

Return the reprint order form by fax or by e-mail with the corrected proofs, to Wiley-VCH : **afm@wiley.com**

To avoid commonly occurring errors, **please ensure that the following important items are correct** in your proofs (please note that once your article is published online, no further corrections can be made):

- **Names** of all authors present and spelled correctly
- **Titles** of authors correct (Prof. or Dr. only: please note, Prof. Dr. is not used in the journals)
- **Addresses** and **postcodes** correct
- **E-mail address** of corresponding author correct (current email address)
- **Funding bodies** included and grant numbers accurate
- **Title** of article OK
- All **figures** included
- **Equations** correct (symbols and sub/superscripts)

Corrections should be made directly in the PDF file using the PDF annotation tools. If you have questions about this, please contact the editorial office. The corrected PDF and any accompanying files should be uploaded to the journal's Editorial Manager site.

Author Query Form

WILEY

Journal ADFM

Article adfm201906205

Dear Author,

During the copyediting of your manuscript the following queries arose.

Please refer to the query reference callout numbers in the page proofs and respond to each by marking the necessary comments using the PDF annotation tools.

Please remember illegible or unclear comments and corrections may delay publication.

Many thanks for your assistance.

Query No.	Description	Remarks
Q-OO	Open access publication of this work is possible via Wiley OnlineOpen. Information about this is available at: https://authorservices.wiley.com/author-resources/Journal-Authors/licensing-open-access/open-access/onlineopen.html. The cost of publishing your manuscript OnlineOpen may be covered by one of Wiley's national agreements. To find out more, visit https://authorservices.wiley.com/author-resources/Journal-Authors/open-access/affiliation-policies-payments/index.html. Note that eligibility for fee coverage is determined by the affiliation of the primary corresponding author designated at submission. Please log in to your Wiley Author Services account at https://authorservices.wiley.com/ and confirm your affiliation to see if you are eligible. Instructions for placing an OnlineOpen order can be found at: https://authorservices.wiley.com/author-resources/Journal-Authors/open-access/how-to-order-onlineopen.html. To publish your article open access, please complete the order process before completing your proof corrections.	
Q1	Please confirm that forenames/given names (blue) and surnames/family names (vermilion) have been identified correctly.	
Q2	Please provide the highest academic title (either Dr. or Prof.) for all authors, where applicable.	
Q3	Please shorten Abstract text to a maximum of 200 words. All abbreviations should be defined.	
Q4	Please shorten Table of Contents text to a maximum of 60 words. All abbreviations should be defined.	

Please confirm that Funding Information has been identified correctly.

Please confirm that the funding sponsor list below was correctly extracted from your article: that it includes all funders and that the text has been matched to the correct FundRef Registry organization names. If a name was not found in the FundRef registry, it may not be the canonical name form, it may be a program name rather than an organization name, or it may be an organization not yet included in FundRef Registry. If you know of another name form or a parent organization name for a "not found" item on this list below, please share that information.

FundRef Name	FundRef Organization Name
Engineering and Physical Sciences Research Council	Engineering and Physical Sciences Research Council
H2020 European Research Council	H2020 European Research Council
UK Regenerative Medicine Platform	
UK Regenerative Medicine Platform Hub Acellular SMART materials 3D architecture	
UK Regenerative Medicine Platform	
EPSRC	Engineering and Physical Sciences Research Council
National Key Research and Development Program of China	National Key Research and Development Program of China
National Natural Science Foundation of China	National Natural Science Foundation of China

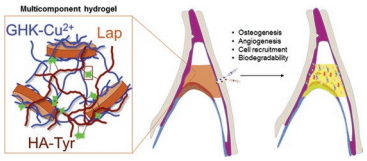

A multicomponent hydrogel platform that combines oxidative coupling with supramolecular coassembly to enable tunability of physical, mechanical, and biological properties desirable in bone tissue regeneration is reported. Specifically, the strategy permits the integration of the osteogenic properties of Laponite (Lap), the nanofibrous structure of peptide amphiphiles, the proangiogenic properties glycyl-histidyl-lysine peptide, and the instant gelation properties of tyramine-modified hyaluronic acid.

ADVANCED FUNCTIONAL MATERIALS
www.afm-journal.de

Growth-Factor Free Multicomponent Nanocomposite Hydrogels That Stimulate Bone Formation

Babatunde O. Okesola, Shilei Ni, Burak Derkus, Carles C. Galeano, Abshar Hasan, Yuanhao Wu, Jopeth Ramis, Lee Buttery, Jonathan Dawson, Matteo D'Este, Richard OC Oreffo, David Eglin, Hongchen Sun,* and Alvaro Mata*

Synthetic osteo-promoting materials that are able to stimulate and accelerate bone formation without the addition of exogenous cells or growth factors will represent a major opportunity for an aging world population. a coassembling system that integrates hyaluronic acid tyramine (HA-Tyr), bioactive peptide amphiphiles (GHK-Cu^{2+}), and Laponite (Lap) is reported to engineer hydrogels with physical, mechanical, and biomolecular signals that can be tuned to enhance bone regeneration. The central design element of the multicomponent hydrogels is the integration of self-assembly and enzyme-mediated oxidative coupling to optimize structure and mechanical properties in combination with the incorporation of an osteo- and angio-promoting segments to facilitate signaling. Spectroscopic techniques are used to confirm the interplay of orthogonal covalent and supramolecular interactions in the multicomponent hydrogels formation. Electron microscopy and analytical techniques are used to confirm coassembly by assessing changes in the nanostructures and elemental compositions of the multicomponent hydrogels. Furthermore, physico-mechanical characterizations reveal that the multicomponent hydrogels exhibit improved compressive strength, stress relaxation profile, low swelling ratio, and retarded enzymatic degradation compared to the single component hydrogels. Applicability is validated in vitro using human mesenchymal stem cells and human umbilical vein endothelial cells, and in vivo using a rabbit maxillary sinus floor reconstruction model. Animals treated with the HA-Tyr-HA-Tyr-GHK-Cu^{2+} hydrogels exhibit significantly enhanced bone formation relative to controls including the commercially available Bio-Oss.

1. Introduction

There is an increasing need to develop strategies to facilitate bone repair and regeneration in and around missing or defective craniomaxillofacial regions, such as eyes, ears, noses, maxilla, mandible, and teeth. One area that requires particular attention, given its anatomical complexity and potential complications, is the posterior maxillary. Here, loss of teeth can result in adverse conditions including severe maxillary sinus pneumatization, which can also increase the risk of root tips, teeth displacement into the sinus cavity, or microbial contamination of the maxillary sinus lift.[1] Therefore, implantation of osseointegrated biomaterials has gained widespread attention in dentistry to replace missing or lost teeth with successful outcomes of complete or partial edentulism.[2] However, due to insufficient alveolar bone and irregular structure of the maxillary sinus in atrophied maxilla, accidental displacement of a dental implant into the maxillary sinus remains a common complication encountered in dental clinical practice.[3] Consequently, maxillary sinus floor reconstruction is

B. O. Okesola, B. Derkus, C. C. Galeano, A. Mata
Institute of Bioengineering
Queen Mary University of London
London E1 4NS, UK

B. O. Okesola, B. Derkus, C. C. Galeano, A. Mata
School of Engineering and Materials Science
Queen Mary University of London
London E1 4NS, UK

S. Ni
Department of Oral Pathology
School and Hospital of Stomatology
Jilin University
Changchun 130000, China

B. Derkus
Biomedical Engineering Department
Faculty of Engineering
Eskisehir Osmangazi University
26040 Eskisehir, Turkey

A. Hasan, Y. Wu, A. Mata
School of Pharmacy
University of Nottingham
Nottingham NG7 2RD, UK

A. Hasan, Y. Wu, J. Ramis, L. Buttery, A. Mata
Biodiscovery Institute
University of Nottingham
Nottingham NG7 2RD, UK

The ORCID identification number(s) for the author(s) of this article can be found under https://doi.org/10.1002/adfm.201906205.

DOI: 10.1002/adfm.201906205

often necessary. Various bone-grafting biological materials including autologous grafts, allogenic bones, and xenografts are routinely used in the clinic to aid bone formation for the sinus floor.[4,5] Notwithstanding, immunogenicity, donor site morbidity, disease transmission, scarcity of donors, and high cost are typically associated with these graft materials.

Significant research efforts have been expended to develop effective bone substitutes for maxillary sinus floor reconstruction.[6] The majority of the studies have focused on the potency of bioceramics including hydroxyapatite, calcium phosphate cements,[7] calcium sulfates,[8] bioactive glasses,[9] and calcium carbonates[10] given their similarity with the inorganic components of natural bone and the ability of these materials to bind to bone and teeth.[11] The success of this approach has resulted in a range of popular, commercially available, hydroxyapatite powders, cements, and granules including: Bio-Oss (Geistlich Ltd., Switzerland) and Fisiograft Bone (Ghimas S.p.A, Italy). In addition, hybridization of inorganic materials with polymers and/or growth factors has been explored as injectable composite materials for craniomaxillofacial bone tissue engineering.[12] Similarly, membranes made from synthetic (*exe*. poly(L-lactic acid) (PLLA), polycaprolactone (PCL))[13,14] or natural (*exe*. collagen, chitosan, alginate)[15,16] polymers have been used to promote bone formation as well as peptides[17] or proteins[18,19] to selectively stimulate relevant processes, such as mineralization. Nonetheless, an ideal bioactive scaffold for maxillary sinus floor reconstruction would enable the possibility to be delivered through minimally invasive means, while rapidly adapting to complex anatomical geometries.[20]

Hydrogels are attractive alternatives to bone grafts given their high water content, porosity for oxygen and nutrient permeability, biocompatibility, and responsiveness to environmental stimuli. Tailored-made hydrogels enable the incorporation of specific bioactive epitopes[21] and exhibit physical properties, such as non-Newtonian behavior to facilitate injectability.[22] However, the use of injectable hydrogels in maxillofacial surgery is limited and in most cases hydrogels have been used mainly as a delivery vehicle for growth factors, such as bone morphogenetic protein-2 (BMP-2) and vascular endothelial growth factor (VEGF).[23–25] Furthermore, while growth factors are efficient promoters of tissue growth, their use is associated with a variety of critical complications, such as the need for large amounts of growth factors due to the rapid inactivation and clearance of the growth factors,[26] high-costs, and uncontrolled activity.[27]

Thus, an ideal therapeutic hydrogel for maxillary sinus lift reconstruction/augmentation should also be biodegradable generating nontoxic products, be simple to implant, exhibit a short set time, be mechanically stable, and rapidly fill irregular anatomical volumes.[28] Furthermore, given the complex anatomy and physiology of bone, the hydrogel should hold multifunctional properties to recreate key features of the extracellular matrix (ECM) and stimulate cell types of interest. In this context, multicomponent self-assembly offers an attractive avenue to design hydrogels with multiple building-blocks, functionalities, and the molecular precision of self-assembly.[29,30]

In this study, we have developed a three-component self-assembling system that integrates hyaluronic acid (HA), peptide amphiphiles (PAs), and Laponite (Lap). HA is a large ECM polysaccharide ubiquitous in tissues and organs that has been extensively used as a biomaterial due to its biocompatibility and biodegradability.[31] However, HA exhibits poor structural integrity and stability and consequently is usually chemically modified with, for example, tyramine (Tyr)[32] or hybridized with other biomaterials, such as hydroxyapatite[33] to increase its functionality. PAs are a class of self-assembling peptide-based building blocks with the intrinsic capacity to assemble into well-defined nanofibrous hydrogels.[34] PAs consist of: i) a hydrophobic tail that drives self-assembly, ii) a β-sheet forming amino acid sequence that stabilizes the assembled nanofibers through hydrogen bonds, and iii) a charged functional head group that facilitates solubility in aqueous environments. This platform can incorporate a spectrum of bioactive epitopes, which have been used to target regeneration of tissues, such as bone,[35] enamel,[36] cartilage,[37] and vascular.[38] However, self-assembling materials typically provide limited structural integrity, which has hindered their wide spread applicability. Lap is a 2D nanosilicate with anisotropic charge distribution, which has been exploited as an effective cross-linker and rheology modifier for hydrogels[39] for the delivery of drugs, growth factors, and antibodies.[40,41] Lap has been reported to promote cell adhesion and proliferation and can exert osteogenic effects on cells in vitro.[42] Consequently, Lap has been combined with macromolecules, such as DNA[43] or proteins[44] to fabricate hydrogels capable of promoting osteogenic differentiation in vitro[45,46] or bone regeneration in vivo in mice.[44]

Here, we report the synthesis and characterization of a multicomponent self-assembling system that integrates the osteogenic properties of Lap, the signaling and nanofibrous structure of PAs, the proangiogenic properties of the GHK-Cu^{2+} peptide, and the biocompatibility and instant gelation properties of Tyr-modified HA to fabricate an osteoinductive and osteoconductive hydrogel for bone regeneration. The system also takes advantage of both covalent (oxidative coupling) and noncovalent (electrostatic) interactions to generate a material that is both injectable and robust. The applicability of the materials was assessed in vitro using human mesenchymal stem cells (hMSCs) and human umbilical vein endothelial cells (hUVECs), and in vivo using a rabbit maxillary sinus floor reconstruction model.

J. Dawson, R. OC Oreffo
Bone and Joint Research Group
Centre for Human Development
Stem Cells and Regeneration
Institute of Developmental Sciences
University of Southampton
Southampton SO16 6YD, UK
M. D'Este, D. Eglin
AO Research Institute Davos
Clavadelerstrasse 8, 7270 Davos Platz, Switzerland
H. Sun
Department of Oral and Maxillofacial Pathology
School and Hospital of Stomatology
China Medical University
Shenyang 110000, China
E-mail: hcsun@jlu.edu.cn
A. Mata
Department of Chemical and Environmental Engineering
University of Nottingham
Nottingham NG7 2RD, UK
E-mail: a.mata@nottingham.ac.uk

2. Results and Discussion

2.1. Rationale of Design

Our approach enables the rationale design of complex and multifunctional hydrogels for bone regeneration (**Figure 1**a–d). We used HA to provide a rich and biocompatible ECM macromolecule, which was functionalized with Tyr (**HA-Tyr**) to control stability through enzyme-mediated oxidative coupling as previously described by Eglin and co-workers.[47] To further enhance the hydrogel's structural integrity and bioactivity, we designed PA molecules to coassemble with **HA-Tyr** through electrostatic interactions into nanofibers that exhibit the proangiogenic osteonectin fragment glycine-histidine-lysine (**GHK-Cu^{2+}**).[48] In addition, Laponite discs (**Lap**) were incorporated to provide a distinctive dual-charged structure (i.e., positive rim and negative face charge of the nanaosilicate disc) that would facilitate interaction with both the anionic charged **HA-Tyr** and the cationic PA (**GHK-Cu^{2+}**). It is noteworthy that the osteogenic effects of **Lap** can be an additional benefit. Finally, to facilitate temporal control of assembly and implantation, the hydrogels were designed to assemble instantly through; a) oxidative coupling of the phenolic moiety of **HA-Tyr** mediated by horseradish peroxidase and H_2O_2, which has been demonstrated to be biocompatible both in vitro and in vivo,[49] as well as b) electrostatic interactions between the cationic **GHK-Cu^{2+}**, anionic **HA-Tyr**, and anionic/cationic **Lap**.

2.2. Synthesis and Characterization of the GHK-Cu^{2+} PA

The PA molecule (**GHK-Cu^{2+}**) used in this study is a three-domain molecule with a hydrophobic tail (black), β-sheet forming amino acid residues (blue), and the therapeutic cationic tripeptide matrikine (pink) derived from osteonectin ($C_{16}H_{31}$CO-VVVAAAGHK) (Figure 1b). In order to present GHK as a complex of copper (the form in which it exists in the human body), we mixed an aqueous solution of copper (II) sulfate ($CuSO_4$. $5H_2O$) (4 mg mL^{-1}) with a GHK solution (2 wt%). The copper chelating ability (**GHK-Cu^{2+}**) was confirmed by electron paramagnetic resonance (EPR) spectroscopy (Figure S1, Supporting Information). The circular dichroism (CD) spectrum of **GHK-Cu^{2+}** demonstrated a β-sheet-like bisignate with a maximum and minimum at 198 and 220 nm, respectively (Figure S2, Supporting Information), while transmission electron microscopy (TEM) confirmed self-assembly into the classical PA nanofibrous morphology measuring ≈10 nm in diameter and several microns in length (Figure S3, Supporting Information).

2.3. Synthesis and Characterization of the Hydrogels

The multicomponent system (**HA-Tyr-Lap-GHK-Cu^{2+}**) was prepared in stages. First, a **HA-Tyr** solution (6 wt%) in horseradish peroxidase (HRP)-containing phosphate buffer saline

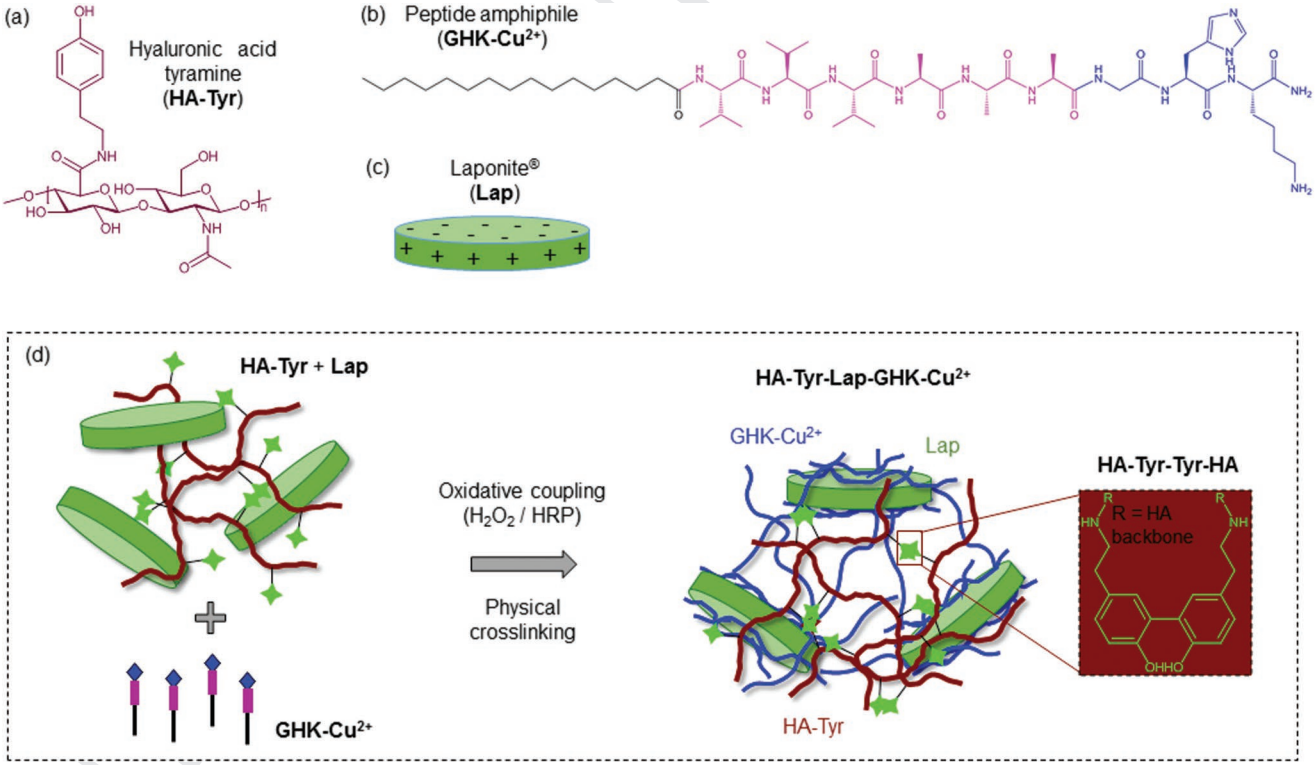

Figure 1. a) Structural formula for hyaluronic acid tyramine (**HA-Tyr**), b) Structural formula for peptide amphiphile (**GHK**), c) Structural representation of Laponite (**Lap**) discs. d) Schematic representation of multicomponent coassembly of **HA-Tyr-Lap** mixtures and **GHK-Cu^{2+}** to fabricate nanocomposite hydrogels via orthogonal physical crosslinking between various components and enzyme-mediated oxidative coupling of **HA-Tyr** to form a dityramine moiety.

(PBS) was combined with exfoliated Lap (5 wt%). Separately, an aqueous solution of **GHK-Cu^{2+}** (2 wt%) was combined with H_2O_2 (0.75×10^{-6} M). Upon mixing both solutions, instant gelation occurred by HRP mediated oxidative coupling of the phenolic moiety on **HA-Tyr** using H_2O_2 as oxidant and by electrostatic interactions between the **GHK-Cu^{2+}** with both **Lap** and **HA-Tyr**. The hydrogels **HA-Tyr**, **HA-Tyr-GHK-Cu^{2+}**, and **HA-Tyr-Lap** were prepared as described in the Experimental Section and used as controls. In all cases, self-supported and robust hydrogels were formed (Figure S4, Supporting Information). Due to the multicomponent nature of the hydrogels, these were prepared with fixed concentrations of both **HA-Tyr**[50] and **Lap**[45] that have been previously reported by others to exhibit suitable mechanical properties and bioactivity. We used fluorescence and attenuated total reflectance-Fourier transform infrared (ATR-FTIR) spectroscopies to investigate molecular interactions underpinning coassembly of the various components in our hydrogels. The fluorescence emission spectra of **HA-Tyr** solution and hydrogels prepared by oxidative coupling were examined. Spectra were collected at an excitation wavelength (λ_{ex}) of 260 nm. The fluorescence spectra from **HA-Tyr** solution (0.5 wt%) depicted a weak broad emission maxima (λ_{em}) at 330 nm, which corresponds to the emission wavelength of a phenolic group (Figure S5, Supporting Information). Upon oxidative coupling the spectra shows an intense emission maxima at 422 nm with a shoulder at 450 nm (Figure S5, Supporting Information). The redshifted fluorescence emission is indicative of peroxidase-catalyzed oxidative coupling leading to dityramine/dityrosine bridge formation.[51]

The FTIR spectrum of GHK exhibited a band at 3250 cm^{-1} due to N–H vibrational stretching of amide II, 2952 and 2850 cm^{-1} due to C–H stretching of alkyl groups, 1632 cm^{-1} due to C=O stretching of amide I, 1540 cm^{-1} due to N–H stretching of amide II (aromatic) and 1230 cm^{-1} due to N–H stretching of amide III (Figure S6, Supporting Information). For **HA-Tyr** xerogel, the characteristic absorption bands were observed at 3200, 1638, 1540, and 1020 cm^{-1} corresponding to the O–H vibrational stretching, C=O stretching of amide I, N–H stretching of amide II, and C–O asymmetric vibrational stretching, respectively (Figure S6, Supporting Information). The distinctive absorption band at 993cm^{-1} in the spectrum of Lap was attributed to the Si–O vibrational stretching.[45] In the spectrum of **HA-Tyr-GHK-Cu^{2+}** xerogel, we observed a slight shift in the vibrational stretching frequency of the C=O region to 1635 cm^{-1}, suggesting hydrogen bond with associated electrostatic interactions between **HA-Tyr** and GHK-Cu^{2+}. Similarly, the spectrum of **HA-Tyr-Lap** xerogel shows that the C=O and Si–O bands shifted to 1635 and 1000 cm^{-1}, respectively, which is indicative of hydrogen bond interactions between **HA-Tyr** and Lap. Interestingly, all the changes observed in the chemical environments of the functional groups (see **HA-Tyr-GHK** and **HA-Tyr-Lap**) were also revealed in the spectrum of the multicomponent **HA-Tyr-Lap-GHK-Cu^{2+}** xerogels. Given the evidence of the peroxidase-mediated oxidative coupling of **HA-Tyr** and the electrostatic and hydrogen bond interactions provided by **Lap** and the cationic **GHK-Cu^{2+}**, we reasoned that the synthesis of our multicomponent **HA-Tyr-Lap-GHK-Cu^{2+}** hydrogels is based on orthogonal interactions between all the components.

2.4. Structural Properties of the Hydrogels

Scanning electron microscopy (SEM) observations revealed that the **GHK-Cu^{2+}** hydrogel exhibited the classical PA nanofibrous architecture[34] (**Figure 2**a), while the **HA-Tyr** hydrogel exhibited a microporous morphology (Figure 2b) as previously described.[52] As expected, **HA-Tyr-GHK-Cu^{2+}** hydrogels exhibited features of both of these hydrogels including nanofibers and microscopic pores (Figure 2c). The multicomponent **HA-Tyr-Lap-GHK-Cu^{2+}** hydrogels revealed an architecture that combined and retained all these features (Figure 2e) with **Lap** uniformly distributed on the surface of the fibers (Figure 2f), as evidenced by energy dispersive X-ray (EDX) analysis confirming the presence of Si, Mg, Na, and O (Figure 2g). Although SEM examinations are not the ideal approach to describe in detail the structure of each hydrogel given the likelihood for structure disruption as a result of the sample preparation, the results provide a useful relative comparison between the different hydrogels.

2.5. Mechanical and Physical Properties of the Hydrogels

A major goal of our design was to provide a multifunctional bioactive hydrogel that could stimulate specific biological processes while being a robust and easy to use system. To test the structural and mechanical properties of the hydrogels, we performed a number of tests including compressive tests, stress relaxation measurements, swelling tests, and enzymatic degradation experiments.

Compression tests were performed on 5 mm diameter and 5 mm high cylindrical hydrogels. **HA-Tyr** hydrogels exhibited a Young's modulus of 25.03 ± 4.00 (Figure 2h; and Figure S7, Supporting Information), in agreement with those of previous studies.[50] Interestingly, upon co-assembly with **GHK-Cu^{2+}** the Young's modulus of the hydrogel increased slightly up to 28.18 ± 4.32 kPa (**HA-Tyr-GHK-Cu^{2+}**), which may result from an enhanced entanglement with the PA nanofibers and consequent slight decrease in porosity (Figure 2c). Importantly, upon coassembly with **Lap**, the hydrogels exhibited a significantly increase in Young's moduli up to 58.23 ± 7.8 kPa (**HA-Tyr-Lap**) and 63.11 ± 8.0 kPa (**HA-Tyr-Lap-GHK-Cu^{2+}**) (Figure 2h, Figure S7, Supporting Information), indicating that the dityramine moieties (HA—Tyr—Tyr—HA bonds) that result from enzymatic crosslinking of the tyramine form strong physical interfacial bonds with **Lap**. These results are in agreement with previous studies that have reported a Lap-induced increase in the stiffness of hydrogels[53] and evidence the potential of our hydrogels to be used as robust and bioactive hydrogel implants for bone regeneration.

It is well-established that hydrogel stiffness plays a crucial role in directing cell phenotype and that stiffer hydrogels (>30 kPa) are able to promote osteoblastic phenotypes.[54] While the Young's modulus of our multicomponent **HA-Tyr-Lap-GHK-Cu^{2+}** hydrogel is higher (63.11 kPa), differences in stiffness measuring techniques and other hydrogel properties such as porosity and stress relaxation are important to consider. In addition to the effect of hydrogel stiffness on cell behavior, stress relaxation has also been shown to play a role in cell signaling

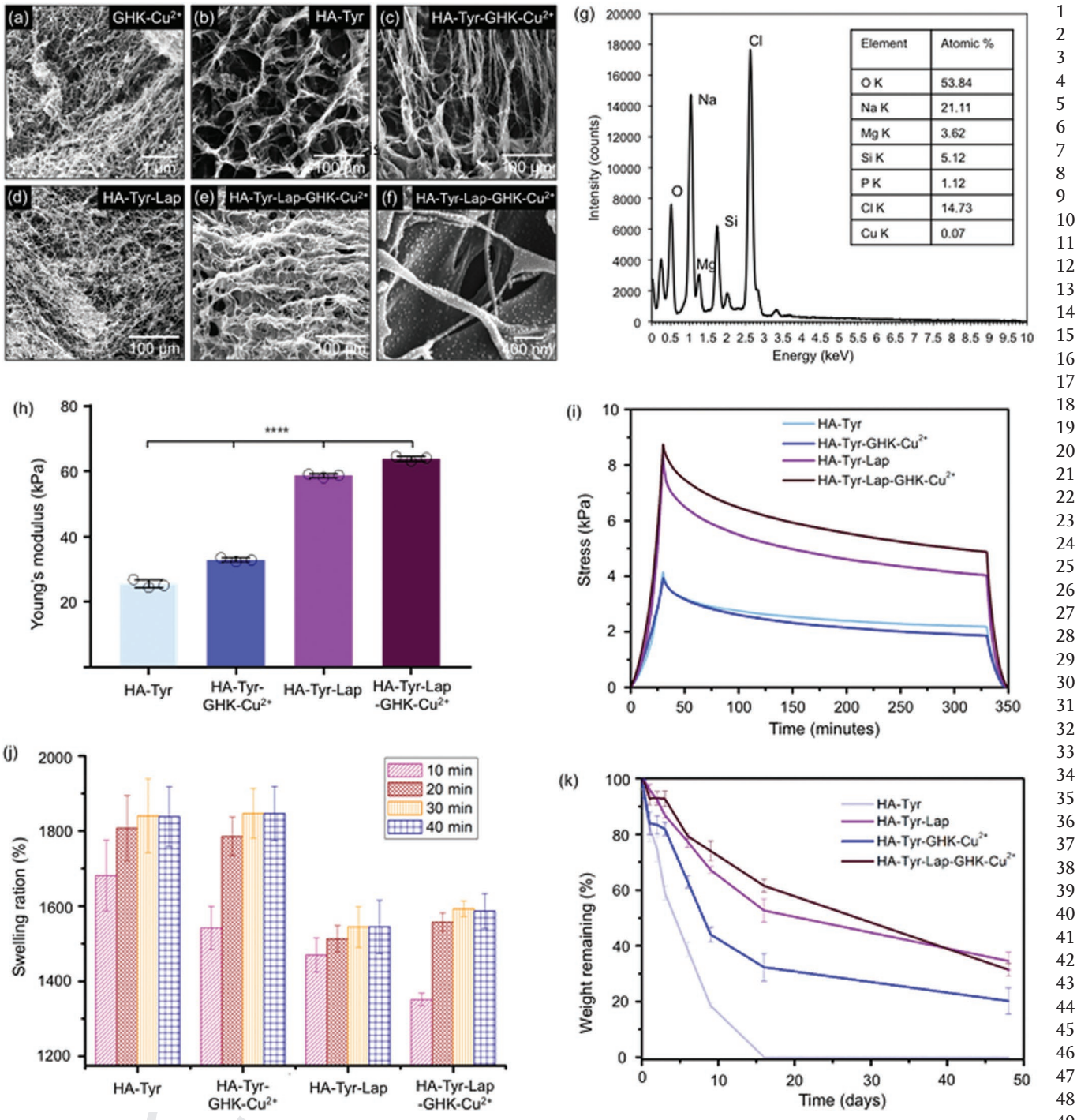

Figure 2. SEM micrographs of dried xerogels of a) **GHK-Cu^{2+}**, b) **HA-Tyr**, c) **HA-GHK- Cu^{2+}**, d) **HA-Tyr-Lap**, e) **HA-Tyr-Lap-GHK-Cu^{2+}**, and f) close image of **HA-Tyr- Lap-GHK-Cu^{2+}** revealing Lap nanoparticles. g) EDX elemental analysis of dried xerogels of **HA-Tyr-Lap-GHK-Cu^{2+}**. h) Young's moduli for **HA-Tyr**, **HA-Tyr-GHK-Cu^{2+}**, **HA-Tyr-Lap**, and **HA-Tyr-Lap-GHK-Cu^{2+}** hydrogels. i) Stress relaxation profiles for **HA-Tyr**, **HA- Tyr-GHK-Cu^{2+}**, **HA-Tyr-Lap**, and **HA-Tyr-Lap-GHK-Cu^{2+}** hydrogels. j) Swelling ratio of **HA-Tyr**, **HA-Tyr-GHK-Cu^{2+}**, **HA-Tyr-Lap**, and **HA-Tyr-Lap-GHK-Cu^{2+}** hydrogels. k) Enzymatic degradation profiles for **HA-Tyr**, **HA-Tyr-GHK-Cu^{2+}**, **HA-Tyr-Lap**, and **HA-Tyr-Lap-GHK-Cu^{2+}** hydrogels. A fixed concentration (2 wt%) of **GHK-Cu^{2+}** was used in all cases.

by modulating ligand binding and cytoskeletal organization.[55] Stress relaxation tests revealed that all multicomponent hydrogels and **HA-Tyr** exhibited a similar relaxation profile of ≈55% at about 5 min (Figure 2i). This behavior is likely due to reversible transient molecular interactions and reorganization of the HA chains and/or PA nanofibers as well as release of entanglements driven by in situ formation of dityrosine bridges between adjacent tyramine moieties in the HA-Tyr chains. However, in

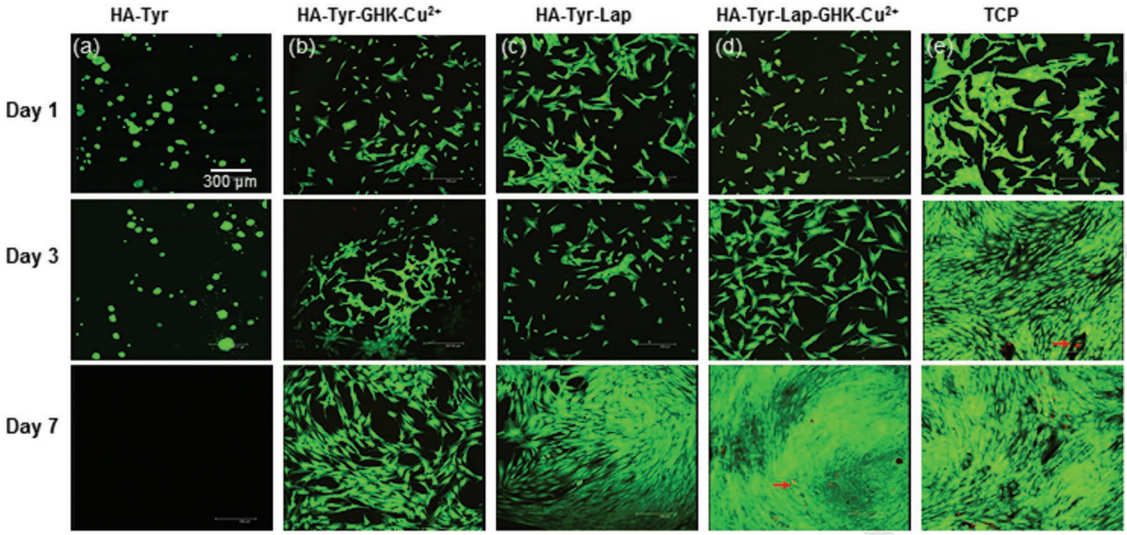

Figure 3. Live/dead assay images of hMSCs seeded on a) **HA-Tyr**, b) **HA-Tyr-GHK-Cu^{2+}**, c) **HA-Tyr-Lap**, d) **HA-Tyr-Lap-GHK-Cu^{2+}** hydrogels, and e) **TCP**.

the initial the 10 s, **HA-Tyr-Lap-GHK-Cu^{2+}** hydrogels exhibit a faster relaxation profile compared to all other hydrogels (Figure 2i). This rapid hydrogel stress relaxation has been shown to promote proliferation and differentiation toward an osteoblastic phenotype of mesenchymal stem cells (MSCs).[55] These results demonstrate that the multicomponent covalent and noncovalent approach also generates a hydrogel relaxation profile with potential benefit for bone regeneration applications.

The propensity of hydrogels to absorb and retain water provides a measure of structural integrity and adaptability as well as capacity to enable critical nutrient and waste diffusion. Consequently, we conducted swelling experiments on freeze-dried hydrogels by immersing them in PBS and systematically calculating the percentage of water uptake at 0, 10, 20, 30, and 40 min. **HA-Tyr** hydrogels exhibited an exceptionally high swelling ratio of 1680 ± 94% after 10 min of immersion in PBS, which increased to 1840 ± 87% after 40 min (Figure 2j). Similarly, **HA-Tyr-GHK-Cu^{2+}** hydrogels displayed a high swelling ratio of 1540 ± 57% which increased to 1802 ± 51%, after 40 min. In contrast, **Lap**-containing hydrogels exhibited lower swelling ratios of 1470 ± 45% (**HA-Tyr-Lap**) and 1350 ± 17% (**HA-Tyr-Lap-GHK-Cu^{2+}**) after 10 min of incubation, which increased to 1540 ± 35% (**HA-Tyr-Lap**) and 1580 ± 24% (**HA-Tyr-Lap-GHK-Cu^{2+}**) after 40 min (Figure 2j). This decrease suggests that despite the ionic and hydrophilic nature of **Lap**, its presence impedes water uptake. Since the degree of swelling ratio is inversely proportional to the crosslinking density of hydrogels,[56] we reasoned that both the physical crosslinking provided by the **Lap** discs and covalent crosslinking between the tyramine moieties (HA—Tyr—Tyr—HA bonds) significantly limit water uptake in **HA-Tyr-Lap** and **HA-Tyr-Lap-GHK-Cu^{2+}** hydrogels. Nonetheless, all hydrogels exhibited a relatively fast and high level of equilibrium swelling ratio, returning to their original size upon rehydration (Figure 2j). This capacity may facilitate their use as geometrically customized hydrogels that can be dried, stored, and rehydrated prior to implantation.

Controlled degradation is another important parameter for bioactive implantable hydrogels aiming to balance stimulation of cell growth and adequate replacement of new tissue. While HA has been extensively pursued as a biomaterial, its use to fabricate robust scaffolds for tissue regeneration has been limited in large part by its susceptibility to rapid degradation in the presence of hyaluronidases both in vitro and in vivo.[57] Several approaches have been devised to enhance HA hydrogel stability to enzymatic degradation with varying degree of success.[58,59] Our design enables the possibility to combine covalent and noncovalent interactions as well as exploit synergistic interactions between the different components. To test this, hydrogels were prepared, immersed in aqueous solutions of hyaluronidase (20 U mL^{-1}) at 37 °C, and their weight measured at various times points up to 50 d (Figure 2k). At 18 d, **HA-Tyr** hydrogels were found to be completely digested, while the multicomponent (**HA-Tyr-GHK-Cu^{2+}**, **HA-Tyr-Lap**, and **HA-Tyr-Lap-GHK-Cu^{2+}**) hydrogels resisted full degradation up to 50 d (Figure 2k). In particular, **Lap**-containing hydrogels exhibited a significant decrease in degradation rate, which correlates with previous studies also reporting an enhanced Lap-induced stability in polymers[60] and biopolymers.[45] We speculate that the suppressed hydrogel susceptibility to rapid enzymatic degradation observed in **HA-Tyr-Lap** and **HA-Tyr-Lap-GHK-Cu^{2+}** may be attributed to the strong affinity of **Lap** discs to proteins and enzymes through physical adsorption,[41] which would consequently limit hyaluronidase access to the HA backbone.

2.6. In Vitro Assessment of the Hydrogels

2.6.1. Viability and Proliferation of hMSCs

To test the applicability of the multicomponent hydrogels, we first conducted in vitro tests by culturing hMSCs on the materials. Using a live/dead assay, cytocompatibility was first assessed. As expected, **HA-Tyr** alone did not support cell attachment and spreading (**Figure 3**), likely as a result of lack of cell-binding motifs.[52] However, cells cultured on all multicomponent **HA-Tyr-GHK-Cu^{2+}**, **HA-Tyr-Lap**, and **HA-Tyr-Lap-GHK-Cu^{2+}** hydrogels adhered and appeared to exhibit a spread

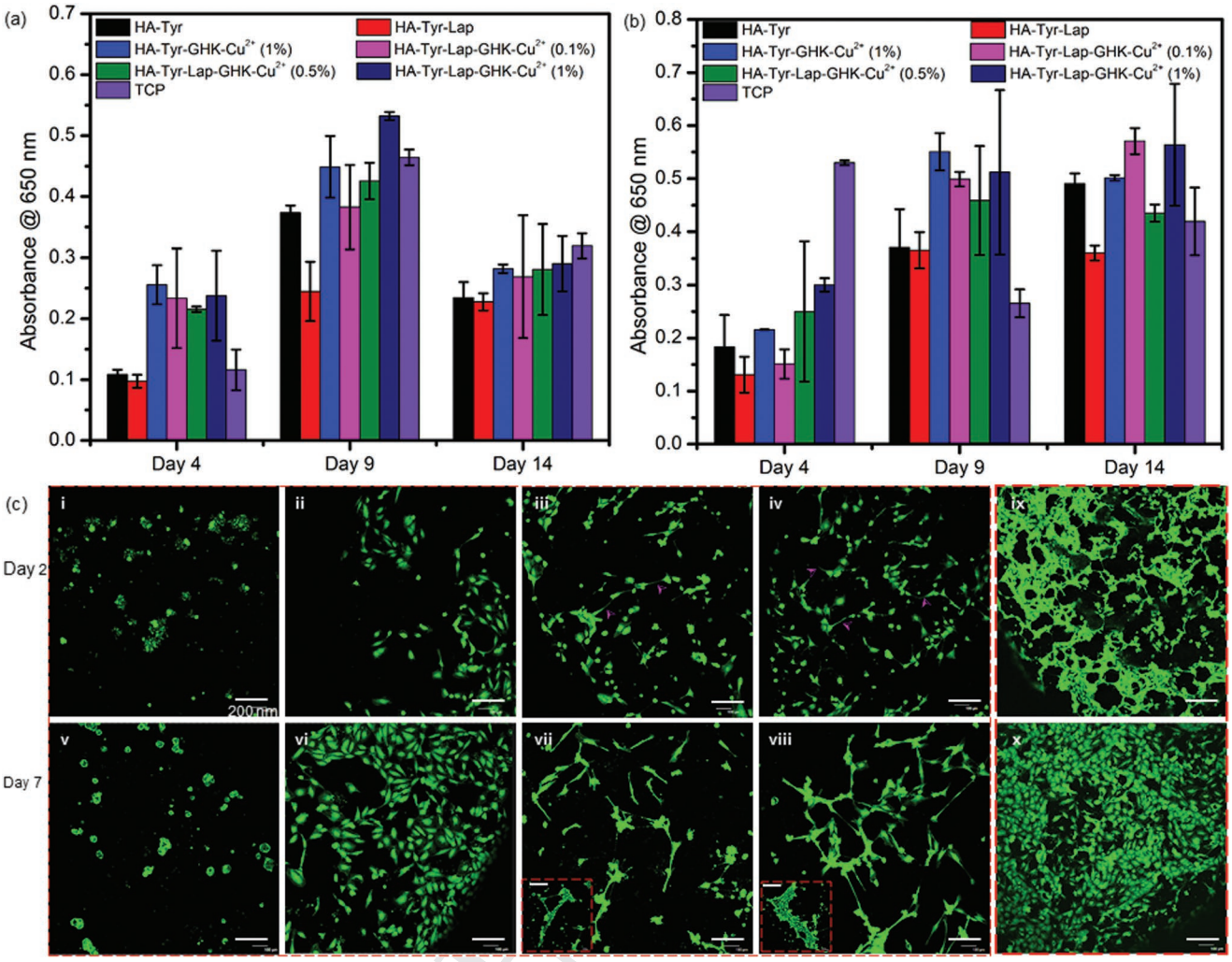

Figure 4. a) Quantitative measurement of cell proliferation on **HA-Tyr**, **HA-Tyr-GHK-Cu^{2+}**, **HA-Tyr-Lap**, **HA-Tyr-Lap-GHK-Cu^{2+}** hydrogels, and **TCP**. b) Osteogenic differentiation of hMSCs without osteoinductive media on **HA-Tyr**, **HA-Tyr-GHK-Cu^{2+}**, **HA-Tyr-Lap**, **HA-Tyr-Lap-GHK-Cu^{2+}** hydrogels, and **TCP** (*, **, ***, **** indicate significant difference with respect to the color code, $p = 0.01–0.001$, $p < 0.001$, $p = 0.001–0.0001$, and $p < 0.0001$, respectively). c) CLSM images of calcein-stained hUVECs at day 1 on (i) **HA-Tyr**, (ii) **HA-Tyr-Lap**, (iii) **HA-Tyr-GHK-Cu^{2+}**, and (iv) **HA-Tyr-Lap-GHK-Cu^{2+}** hydrogels and day 5 on (v) **HA-Tyr**, (vi) **HA-Tyr-Lap**, (vii) **HA-Tyr-GHK-Cu^{2+}** (inset: large lumen), (viii) **HA-Tyr-Lap-GHK-Cu^{2+}** hydrogels, (ix) Matrigel-VEGF (50 ng mL^{-1}), and (x) TCP. Insets of (vii) and (viii) are other lumen structures found on the hydrogels.

morphology (Figure 3b–d) on days 1, 3, and 7 similar to cells cultured on tissue culture plastic (TCP) (Figure 3e). We then examined the effect of the hydrogels on hMSC proliferation and found that cell number increased from day 1 to 7 on all multicomponent hydrogels, with greater increase on **HA-Tyr-Lap-GHK-Cu^{2+}** compared to **HA-Tyr-Lap** and **HA-Tyr-GHK-Cu^{2+}**. In addition, cell proliferation was higher on **HA-Tyr-Lap-GHK-Cu^{2+}** prepared with the higher concentration of GHK-Cu^{2+} (1 wt%) compared to the lower one (0.1 wt%) (**Figure 4**a), which is in agreement with previous work reporting the stimulating role of GHK on cell proliferation.[61]

2.6.2. Osteoblastic Differentiation of hMSCs

Next, we assessed the osteoinductive potential of the multicomponent hydrogels by growing hMSCs using culture media with and without osteoinductive agents and quantifying alkaline phosphatase (ALP) expression. In this case, we tested three different hydrogels comprising different concentrations of **GHK-Cu^{2+}**. In osteoinductive media, up-regulation of ALP activity was observed on all hydrogels with highest expression at day 4 on the TCP control compared to day 9 for the multicomponent hydrogels, suggesting a delayed expression on the hydrogels (Figure S9, Supporting Information). However, in the absence of osteoinductive media, a more indicative scenario of the inductive properties of the materials, ALP expression peaked for all tested substrates on day 9. In this case, the highest expression was observed on the **HA-Tyr-Lap-GHK-Cu^{2+}** hydrogels containing the highest concentration of **GHK-Cu^{2+}** compared to all other hydrogels and TCP control (Figure 4b). This result suggests that the multicomponent **HA-Tyr-Lap-GHK-Cu^{2+}** hydrogel has the capacity to stimulate osteoblastic differentiation on hMSCs in the absence of osteoinductive

factors. Furthermore, the dose-dependent effect of **GHK-Cu^{2+}** on ALP activity is in agreement with previous reports on the osteogenic effect of copper-free alginate-GHK hydrogels.[61]

2.6.3. Angiogenic Effect on hUVECs

Blood vessel formation is essential in bone regeneration. Therefore, we qualitatively assessed the in vitro proangiogenic effect of the multicomponent hydrogels on hUVECs. By comparing the morphology of calcein-stained hUVECs growing on the different materials, **GHK-Cu^{2+}**-containing multicomponent hydrogels **HA-Tyr-GHK-Cu^{2+}** and **HA-Tyr-Lap-GHK-Cu^{2+}** were observed to trigger cell elongation and angiogenic sprouting with microcapillary-like structures by day 1 of culture (Figure 4c_(iii–iv)). In contrast, cells seeded on **HA-Tyr** and **HA-Tyr-Lap** (without **GHK-Cu^{2+}**) maintained their normal endothelial phenotype (Figure 4c_(i–ii). In addition, a more complex vascular lumen[62] structure was also formed on the **GHK-Cu^{2+}**-containing hydrogels after day 5 (Figure 4c_(vii–viii)). Such lumen structures were similar to those observed on the positive control (Matrigel + 50 ng mL^{-1} VEGF) (Figure 4c_(ix)) at day 5. These results suggest that the **GHK-Cu^{2+}-**containing multicomponent hydrogels have proangiogenic properties.

The proangiogenic effects and ability of GHK to increase VEGF secretion have been previously associated with its binding to α_6 or β_1 integrin or both.[63] Also, a recent metabolomics pathway analysis of cells in alginate-GHK hydrogels revealed that the integrin linked kinase mediates the numerous biological functions of GHK tripeptide.[61] The formation of vascular system is mainly ensured by the emergence of new microcapillary from existing vessels (sprouting).[64]

2.7. In Vivo Assessment of the Hydrogels

To test the bioactivity and in vivo bone regenerative capacity of the hydrogels, experiments were conducted on a standard sinus rabbit model following established protocols.[65] The four hydrogel materials were tested with untreated animals serving as negative controls and animals treated with the commercial product Bio-Oss (Geistlich Ltd., Switzerland) as positive controls. Bio-Oss is a bone substitute material derived from deproteinized bovine bone marrow and has been widely used in regenerative dentistry with good success as a filler for maxillary sinus augmentation.[6] Animals were implanted with 50 µL of the hydrogels or positive control, sacrificed at either 6 or 12 weeks after implantation, and assessed qualitatively and quantitatively for bone formation and cytotoxicity.

All animals survived surgery and exhibited normal behavior during the implantation time and no signs of inflammation or infection were physically observed at the time of sacrifice. Cone beam computer tomography (CBCT) was used to qualitatively assess differences in the performance of the different materials. At 6 and 12 weeks, CBCT scans revealed new bone formation in the sinus of animals treated with the hydrogels and positive control (Bio-Oss) (**Figure 5**b). However, higher contrast likely associated with new bone formation was observed in animals treated with the multicomponent hydrogels, especially those treated with the **HA-Tyr-Lap-GHK-Cu^{2+}** hydrogels. Interestingly, this enhancement also appeared to be larger than animals treated with the positive control at both 6 and 12 weeks' time-points. It is noteworthy that the radiation resistant area in the sinus of the positive control is partly due to the residual materials of the Bio-oss, which can be difficult to distinguish from the newly mineralized tissue. Nonetheless, the results suggest that the **HA-Tyr-Lap-GHK-Cu^{2+}** hydrogels are capable of promoting new bone formation within the sinus.

To confirm this result, histological sections stained with hematoxylin and eosin (HE) were acquired from animals at 6 and 12 weeks after implantation. Animals implanted with the **HA-Tyr-Lap-GHK-Cu^{2+}** hydrogels qualitatively exhibited greater amounts of newly formed bone compared to animals treated with all other hydrogels and controls at both weeks 6 and 12, evidenced by the presence of relevant cells and ossified tissue (Figure 5c). These histological sections were then used to quantify new bone formation within the sinus region by identifying and quantifying the areas within the sinus region exhibiting osteocytes and ossified tissue (Figure 5a). At both 6 and 12 weeks postsurgery, the results confirmed that animals receiving the multicomponent **HA-Tyr-Lap-GHK-Cu^{2+}** hydrogels revealed the highest percentage of mean area of ossified tissue (40.37 ± 1.54 and 60.12 ± 2.80%, respectively) within the sinus of all tested groups including significantly higher than animals treated with the positive control (35.97 ± 1.54% and 37.56 ± 1.18%, respectively) (**Figure 6**a). The histological sections of animals treated with the **HA-Tyr-Lap-GHK-Cu^{2+}** hydrogels also exhibited both osteoblasts and osteocytes within lacuna, further evidencing the presence of an active regenerative environment (Figure 6b). It is likely that these cells emerged from MSCs or preosteoblasts migrating from the local bone surface, periosteum, or the blood. By comparing these results with those of the other hydrogels (Figure 6a), we conclude that the enhanced bioactivity of **HA-Tyr-Lap-GHK-Cu^{2+}** hydrogels may result primarily from the presence of **Lap** and **GHK-Cu^{2+}**. These results correlate with the in vitro results, which show that Lap and especially GHK may have osteoinductive properties in the absence of growth factors. Vascularization is of upmost importance in bone regeneration. Closer examination of the histological sections revealed that animals treated with **HA-Tyr-Lap-GHK-Cu^{2+}** exhibited a qualitatively higher amount of blood vessels compared to animals treated with **HA-Tyr-GHK-Cu^{2+}** and the positive control (Figure 6c). Interestingly, blood vessels were much less prevalent in hydrogels that did not contain **GHK-Cu^{2+}**, which is in accordance with the in vitro experiments as well as previous studies that have reported on the ability of GHK-Cu^{2+} to promote formation of blood vessels in mice.[66] The in vivo experiments were also used to investigate the biosafety of the hydrogels through a systemic toxicity test. Histological sections of the liver, heart, spleen, lung, and kidney from the animals treated with the **HA-Tyr**, **HA-Tyr-GHK-Cu^{2+}**, **HA-Tyr-Lap**, and **HA-Tyr-Lap- GHK-Cu^{2+}** hydrogels were examined and presented no signs of inflammation or histological changes compared to control animals (Figure S11, Supporting

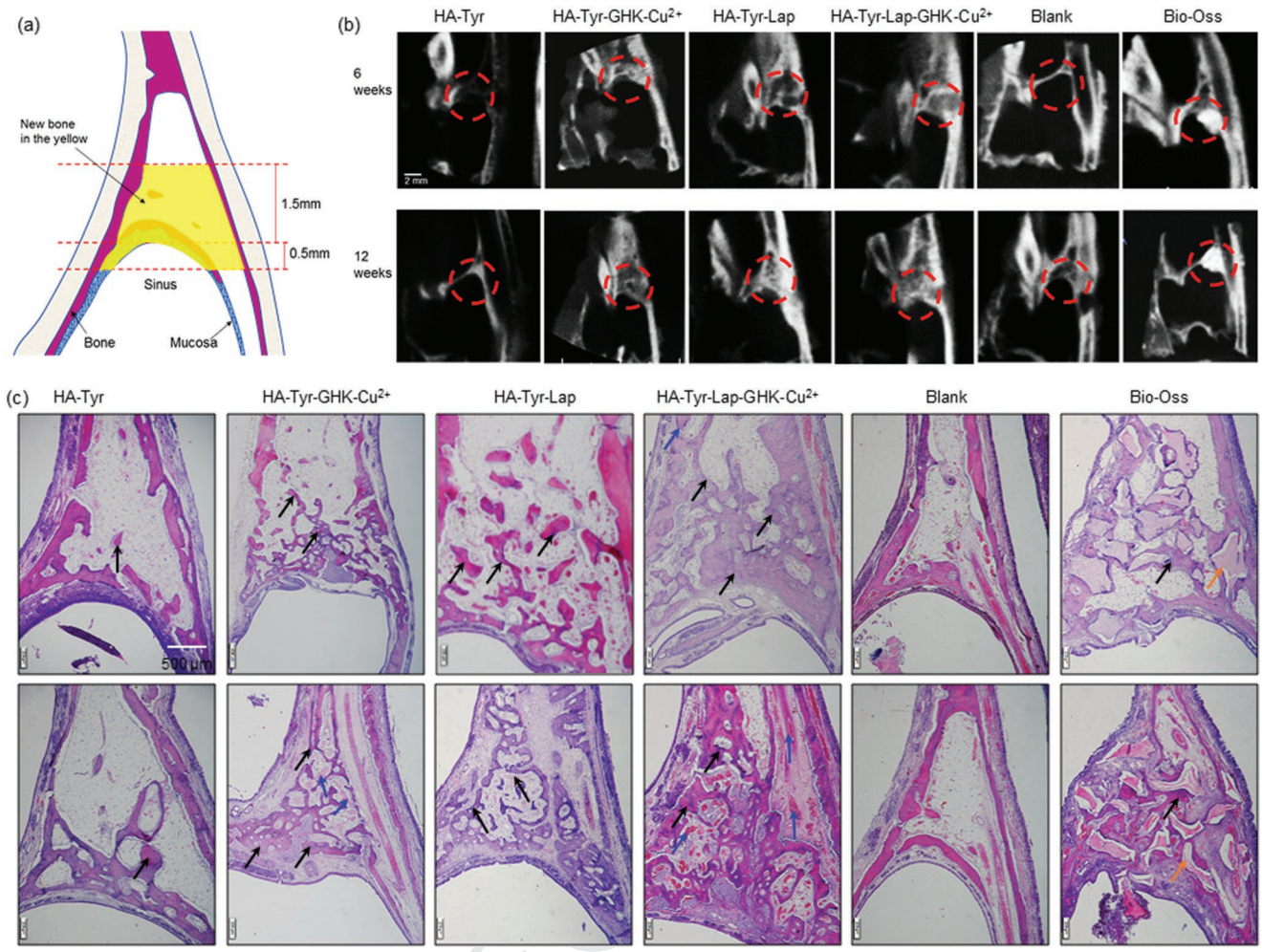

Figure 5. a) Schematic representation of new bone area in the maxillary sinus. b) Cone beam computed tomography (CBCT) scan results of sinus floor treated with **HA-Tyr**, **HA-Tyr-GHK-Cu^{2+}**, **HA-Tyr-Lap**, and **HA-Tyr-Lap-GHK-Cu^{2+}** hydrogels compared with sinus treated with nothing and those treated with Bio-Oss after 6 and 12 weeks postsurgery. c) New bone formation detected by hematoxylin and eosin (HE) staining shows local histological images of the different groups at 6 and 12 weeks postsurgery, respectively. The black, blue, and orange arrows indicate the new trabecular bone and blood vessels filed with red blood cells and residual Bio-Oss.

Information). These results suggest that the **HA-Tyr-Lap-GHK-Cu^{2+}** hydrogels did not degrade into toxic by-products. We speculate that, beyond the molecular signaling and biocompatibility of the **HA-Tyr-Lap-GHK-Cu^{2+}** hydrogel, its high osteo-promoting activity may also result from the inherent mechanical and physical properties of the hydrogel. Both the hydrogel's Young's modulus (Figure 2h) and stress relaxation profile (Figure 2i) exhibit values that have been reported to be beneficial for bone promoting applications.[54,55] Furthermore, the hydrogels display an enzymatic degradation profile (Figure 2k) that may have permitted sufficient signaling to migrating and surrounding cells while progressively degrading to enable new tissue formation. This capacity for timely scaffold degradation is key for optimum tissue regeneration.[67] Furthermore, beyond these beneficial molecular, chemical, and physical properties, the potential to easily manipulate and deliver the hydrogel represent key advantages to facilitate its clinical use and impact.

3. Conclusion

We have developed a practical and multifunctional self-assembling hydrogel biomaterial for bone regeneration applications. The material takes advantage of both covalent and noncovalent interactions to integrate HA, PAs, and Lap into a bioactive hydrogel with a spectrum of molecular, physical, and mechanical properties designed to promote bone regeneration as well as minimally invasive implantation. We demonstrate the capacity of the hydrogels to support cell growth and stimulate both osteoblastic differentiation and angiogenic sprouting of hUVECs in vitro as well as promote faster bone regeneration in a rabbit model compared to a commercially available gold-standard material. The current study introduces a new molecularly designed self-assembling material that stimulates bone formation without the use of exogenous growth factors and demonstrated its potential use in maxillary sinus reconstruction and other bone tissue regeneration procedures.

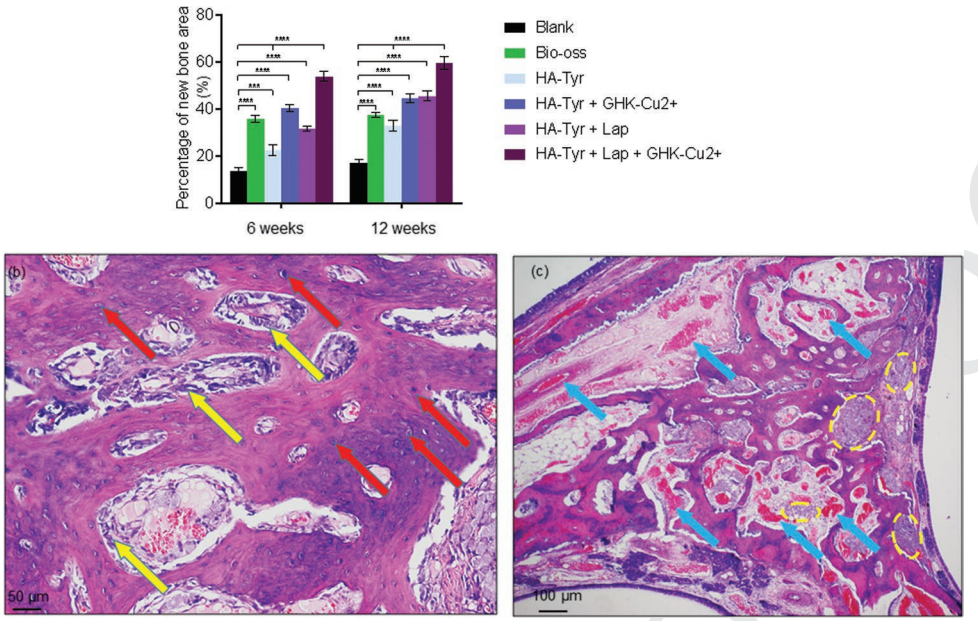

Figure 6. a) Calculated new bone area in the sinus treated with **HA-Tyr**, **HA-Tyr-GHK-Cu^{2+}**, **HA-Tyr-Lap** and **HA-Tyr-Lap-GHK-Cu^{2+}** hydrogels compared with the group treated with nothing (negative control) and those treated with Bio-Oss (positive control) at 6 and 12 weeks (* indicates significant differences, $p < 0.001$). Hematoxylin and eosin staining shows local histological image of the group treated with the multicomponent **HA-Tyr-Lap-GHK-Cu^{2+}** hydrogels at 12 weeks postoperation. b) Histological image showing osteocytes in the trabecular bone (red arrows) and osteoblasts on the surface of the new trabecular bones (yellow arrows) in the group treated with **HA-Tyr-Lap-GHK-Cu^{2+}** hydrogels. c) The blue arrows and yellow circles indicate the blood vessels filed with red blood cells within the new bones and foam cell-like which engulfed the implanted **HA-Tyr-Lap-GHK-Cu^{2+}** hydrogels.

4. Experimental Section

Materials: Laponite XG was a generous gift from the laboratory of Professor Richard OC Oreffo and Dr. Jonathan Dawson, University of Southampton while HA-Tyr was synthesized as previously described elsewhere.[45] Dulbecco's Modified Eagle's Medium (DMEM), fetal bovine serum (FBS), PBS, penicillin, and streptomycin, horseradish peroxidase, hydrogen peroxide were purchased from sigma-Aldrich Inc. (UK). The Live/Dead assay kits (calcein AM and ethidium homodimer) were purchased from Thermo Fisher Scientific Ltd (UK).

Peptide Synthesis and Characterization: PAs were synthesized as previously described[68] by solid phase peptide synthesis on Liberty Blue-automated microwave peptide synthesizer (CEM Ltd, UK). The standard 9-fluorenylmethoxycarbonyl (Fmoc) protection chemistry on a 4-methylbenzhydrylamine (MBHA) Rink Amide resin (Novabiochem Corporation, UK) was employed. Amino acid couplings were performed using 4 mmol equivalent of Fmoc-protected amino acids (Novabiochem Corporation, UK), 4 mmol equivalents of 1-hydroxybenzotriazol (HOBT, Carbosynth Ltd, UK) and 6 mmol equivalents of *N,N'*-diisopropylcarbodiimide (DIC, Sigma-Aldrich Inc., UK) for 1 h. Fmoc deprotections were performed with 20% piperidine (Sigma-Aldrich Inc., UK) in *N,N*-dimethylformamide (DMF, Alfa Aesar Inc., UK). Following Fmoc removal from the final amino acid residue, the alkyl tail moiety (from palmitic acid, $C_{16}H_{32}O_2$, Calbiochem Inc., UK) was conjugated to the free N-terminus. The alkylation reaction was accomplished by using palmitic acid (4 mmol), HOBT (4 mmol), and DIC (6 mmol) in DMF/dichloromethane. The reaction was allowed to proceed at room temperature for 4 h or until obtaining a negative Kaiser test. PA cleavage from the resin and deprotection of the side chains were carried out with a mixture of trifluoracetic acid (TFA, Sigma-Aldrich Inc., UK)/triisopropylsilane (TIS, Alfa Aesar Inc., UK)/water (95:2.5:2.5) for 3 h at room temperature. After filtration of the cleavage mixture, TFA was removed by rota-evaporation and the resulting solution was triturated with cold diethylether at −20 °C. The precipitate was collected by centrifugation, washed twice with cold diethylether, air-dried, dissolve in deionised water and lyophilized. The product was then purified using a preparative HPLC (Waters Ltd, USA) with reverse-phase Xbridge C18 column (Waters Ltd, USA) and water/acetonitrile (0.1% TFA) binary mobile phase. Hydrochloric acid (10×10^{-3} M) was added to the HPLC fractions and rotavap to remove the residual TFA, leaving behind chloride as the PA counter ions. Finally, the PA was dialyzed against deionized water using 500 MWCO dialysis tubing (Spectrum Europe BV, The Netherlands) to remove salts, lyophilized to obtain a white fluffy pure PA. Circular dichroism (CD) was measured with Chirascan circular dichroism spectrometer (Applied Photophysic Ltd, UK) using quartz cell with 1 mm path length and the following parameters: data pitch—0.5 nm, scanning mode—continuous, scanning speed—100 nm min^{-1}, bandwith—2 nm and accumulation—5. All CD data were presented as ellipticity and recorded in millidegree (mdeg). CD spectra were obtained by signal integrating 3 scans, from 190 to 260 nm at speed of 50 nm min^{-1}. Data were processed by a simple moving average and smoothing method. Electron paramagnetic resonance spectroscopy was recorded on a Bruker EMX EPR equipped with a standard cavity, operating at X-band frequency using standard Wilmad quartz tubes at −80 °C. Transmission electron microscopy was performed on etched carbon-coated copper grids (Agar Scientific Ltd, Stanstead, UK) using JEOL 1230 TEM fitted with Morada CCD camera. Samples were stained with aqueous 2% uranyl acetate solution.

Hydrogel Preparation and Characterizations: The requisite concentration (6 wt%) of **HA-Tyr** was prepared in PBS containing 3 unit mL^{-1} of HRP and allowed to fully dissolve overnight at 4 °C. This concentration of **HA-Tyr** was used in all the hydrogel preparations. Gelation of the **HA-Tyr** was triggered by adding aqueous solution of H_2O_2 (0.75×10^{-3} M) and gentle mixing with a pipette tip. In order to prepare **HA-Tyr-GHK-Cu^{2+}** hydrogels, aqueous solution of **GHK-Cu^{2+}** (2 wt%) with 0.4 mg mL^{-1} $CuSO_4$) prepared in H_2O_2 (aq) (0.75×10^{-3} M) was added to **HA-Try**/HRP solution with a quick mixing. To synthesize **HA-Tyr-Lap** hydrogels, aqueous suspension of **Lap** (5 wt%) exfoliated with sodium salt of polyacrylic acid (≈5000 Da M_w, 0.6 wt%) was initially mixed with aqueous solution **HA-Tyr**/HRP followed by the addition of H_2O_2 (aq) (0.75×10^{-3} M). Similarly, **HA-Tyr-Lap-GHK-Cu^{2+}** hydrogels were prepared

by adding aqueous solution of **GHK-Cu^{2+}**/H_2O_2 to **HA-Tyr**/HRP/**Lap** mixture and mixed with a pipette tip.

Molecular Characterization of Coassembly: IR spectra were recorded on a PerkinElmer ATR-FTIR spectrometer in the range of 4000–400 cm^{-1} at 2 cm^{-1} resolution. Fluorescence spectroscopy was carried out on a Hitachi F4500 spectrophotometer. Both excitation and emission slit width was 10.0 nm, scan speed was set to 200 nm min^{-1}.

Unconfined Compression and Stress Relaxation Testing: Elastic moduli *E*o and stress relaxation properties of the hydrogels were measured from the compression tests of the hydrogels with an Instron 560 (Instron, Norwood, MA) using 10 N load cell to a compressive strain of 30% and a deformation rate of 1 mm s^{-1}. The cylindrical hydrogels (diameter = height = 5 mm) were swollen in PBS for 6 h prior measurements and the testing was carried out inside a flat-bottom petri-dish filled with PBS. Prior to the tests, an initial compressive contact of 0.01 N was applied to ensure a complete contact between the hydrogels and the petri-dish. No bulging of the side faces of the hydrogels was observed. The slope of the stress versus strain curve gives *E*o. After the compression test, the strain was held constant for 5 min, while the load was recorded as a function of time. In order to calculate the stress, the force was divided by the area of the hydrogels in the undeformed state. Tests were carried out three times to ensure reproducibility.

Swelling Properties and Enzymatic Digestion of Hydrogels: In order to determine the swelling properties of the hydrogels, the wet hydrogels were first freeze-dried to a constant initial weight (*W*i). The dried xerogels were then incubated in PBS at 37 °C. The wet weights (*W*t) of the hydrogels were measured at various time intervals during incubation until there was no noticeable increase in the weight the wet hydrogels. The percentage swelling of the hydrogels was calculated using the following equation $(W_t - W_i)/W_i \times 100$). Degradation rate of the hydrogels was characterized by incubating the cylindrical hydrogels in PBS (pH = 7.2) for 24 h and then treated with hyaluronidases (20 unit mL^{-1}). The remaining weight of the hydrogels was measured up to 50 h after enzymatic treatment. The weight loss was computed using equation $(W_f - W_i)/W_i \times 100$, where W_i and W_f represent initial and final hydrogel weights, respectively.

Characterization of Microstructures: Microstructure of the hydrogels was observed using SEM. The hydrogels were frozen by liquid nitrogen and lyophilized to obtain dried samples. The dried gels were then sputter-coated with gold (10 nm thick) for 60 s. SEM micrographs of the dried xerogels were acquired on Inspect F50 (FEI Comp, the Netherlands). EDX spectroscopy was also used to analyze the dried gels coated with carbon to obtain elemental compositions of the dried xerogels.

In Vitro Experiments: Live/Dead assay—Live/dead assay was performed using a Live/Dead Cytotoxicity Kit (Thermo Fisher Scientific, UK) hMSCs (5000 cells mL^{-1}) (Thermo Fisher Scientific, UK) seeded on various hydrogels at day 1, 3, and 7. Imaging was performed on an inverted confocal laser scanning microscope (CLSM, Leica, Germany). Proliferation—Cell proliferation was assessed by seeding 5000 hMSCs on various hydrogels. The cell seeded hydrogels were seeded incubated at 37 °C under 5% CO2 condition. Cell proliferation was quantitatively measured at various time points (day 1, 4, and 7) using PrestoBlue reagent (PrestoBlue Cell Viability Reagent, Thermo Fisher Scientific, UK). Briefly, the spent media was removed from each well and the cells were incubated with PrestoBlue reagent solution (100 µL). The cells were incubated for 1 h at 37 °C, away from light. Florescence measurements were carried out with using excitation wavelength of 560 nm and an emission wavelength of 590 nm. Differentiation—Cell differentiation was assessed by seeding 20 000 hMSCs (passage 10) on various hydrogels with and without osteogenic media. Experiments were setup in 4 triplicates. With osteogenic media, cells were first cultured with basal media and replaced with osteogenic media after 1 d. After each time point, cells were fixed using 4% formaldehyde for 10 min and washed thrice with sterile dH2O. Cells were incubated with 100 µL of SIGMAFAST BCIP/NBT reagent (Sigma, UK). ALP activity was spectroscopically quantified after days 4, 9, and 14 by measuring absorbance at 650 nm. Angiogenesis—hUVECs (5000) were seeded on various hydrogels. Cell-seeded hydrogels were incubated with supplemented endothelial cells growth media for 1 and 5 d. Cells were stained with calcein AM (2×10^{-3} M) and optical images were acquired on CLSM (Leica, Germany).

In Vivo Maxillary Sinus Floor Reconstruction Procedure: 30 healthy adult New Zealand rabbits were randomly divided into two study groups (control and experimental groups) for observation at week 6 and week 12. General anesthesia was performed through injection of 3% sodium pentobarbital via the marginal ear vein (1 mL kg^{-1}). After the disappearance of eyelash reflex, the hair in the surgery region was shaved and the region was sterilized by 1% Iodine volts. A 2.5 cm incision on the nasal skin along the midline was made and the periosteum was stripped to expose the nasal bone and nasoincisal suture line. Two round windows at each side of the midline were prepared using bone drill. The windows were 5 mm in diameter and located ≈20 mm anterior to the nasofrontal suture line and 10 mm lateral to the midline. During the osteotomy, sterile saline solution was injected to the drill for continuous cooling and the sinus membrane was carefully protected. The mucosa and periosteum were gently elevated with a periosteum elevator and 50 µL gel was prepared in situ within the space upon the surface of the bone. In the experimental groups, four types of gel, as subgroups, including **HA-Tyr**, **HA-Tyr-GHK-Cu^{2+}**, **HA-Tyr-Lap**, and **HA-Tyr- Lap-GHK-Cu^{2+}** was formed within the space. The space in the positive control group was filled with equal volume of Bio-oss and the space in blank control group was empty. The periosteum and skin were then sutured. Each group consisted of five animals.

Histological and Histomorphomeric Analysis: The animals were euthanized 6 and 12 weeks postsurgery by injecting sodium pentobarbital via the marginal ear vein (100 mg kg^{-1}), and the sinuses were retrieved in blocks. The specimens were immediately fixed with paraformaldehyde (4%) for 48 h and demineralized by soaking them in 15% disodium ethylene diamine tetraacetate for 2 months and then washed in tap water for 15 min. All the specimens were trimmed and put into 70%, 80%, 90%, 95%, 100% ethanol step by step for gradually dehydrate, and finally embedded in paraffin. Longitudinal histological HE slices of 4 µm thickness were obtained to visualize the entire sinus. The sections were observed and digitally captured with a microscopic imaging system composed of a microscope (BX51, Olympus, Japan) and an image processing software, Cell Sens (Olympus, Japan). For the calculation of new bone area, Photoshop (Adobe Inc.) was first used to draw the outline of the new bone and ImageJ Fiji (developed by the National Institutes of Health and the Laboratory for Optical and Computational Instrumentation) was then used to calculate the new bone areas. Five slices were analyzed for each group. Fresh tissue blocks containing main organs including heart, liver, spleen, lung, and kidney were obtained and fixed with 4% paraformaldehyde to prepare HE stained slices analysis.

Statistical Analysis: Statistical comparisons between groups treated with various hydrogels, blank (negative control), and Bio-oss (positive control group) were performed using 2-way ANOVA followed by Bonferroni tests if significant differences were observed using Graph Prism software (San Diego). Tukey's multiple comparison test was used for the cell proliferation and differentiation.

Supporting Information

Supporting Information is available from the Wiley Online Library or from the author.

Acknowledgements

B.O.O. and S.N. contributed equally to this work. The work was supported by the ERC Starting Grant (STROFUNSCAFF) and the UK Regenerative Medicine Platform (UKRMP2) Acellular Smart Materials. R.O. and J.D. gratefully acknowledge funding support from the UK Regenerative Medicine Platform Hub Acellular SMART materials 3D

architecture (MR/R015651/1) and the UK Regenerative Medicine Platform (MR/L012626/1 Southampton Imaging). J.D. thankfully acknowledge EPSRC for a fellowship (EP/L010259/1). H.S. acknowledge funding support from the National Key Research and Development Program of China (No. 2016YFC1102800) and the National Natural Science Foundation of China (No. 81870741). The authors thank Dr. Stephen Thorpe at the School of Engineering and Materials Science, QMUL for help with interpreting the mechanics of the hydrogels. They also thank Dr. Vicente Araullo-Peters and Dr. Roberto Buccafusca at Nanovision and the School of Biological and Chemical Sciences (SBCS), QMUL for technical support.

Conflict of Interest

The authors declare no conflict of interest.

Keywords

bone formation, cranio-maxillofacial surgery, multicomponent self-assembly, nanocomposite hydrogels, nanosilicates, self- assembling peptides

Received: July 30, 2019
Revised: January 3, 2020
Published online:

[1] M. Morawska-Kochman, K. Marycz, K. Jermakow, K. Nelke, W. Pawlak, M. Bochnia, *PLoS One* **2017**, *12*, e0176776.
[2] T. Starch-Jensen, J. D. Jensen, *J. Oral Maxillofac. Surg.* **2017**, *8*, e3.
[3] M. Yan, R. Liu, S. Bai, M. Wang, H. Xia, J. Chen, *Sci. Rep.* **2018**, *8*, 1451.
[4] T. M. Jeong, J. K. Lee, *Maxillofac. Plast. Reconstr. Surg.* **2014**, *36*, 146.
[5] S. Nasr, D. E. Slot, S. Bahaa, C. E. Dörfer, K. M. Fawzy El-Sayed, *J. Craniomaxillofac. Surg.* **2016**, *44*, 1607.
[6] T. Starch-Jensen, A. Mordenfeld, J. P. Becktor, S. S. Jensen, *Implant Dent.* **2018**, *27*, 363.
[7] X. Liu, P. Wang, W. Chen, M. D. Weir, C. Bao, H. K. Xu, *Acta Biomater.* **2014**, *10*, 4484.
[8] A. Dasmah, M. Hallman, L. Sennerby, L. Rasmusson, *Clin. Implant Dent. Relat. Res.* **2012**, *14*, 259.
[9] A. C. Profeta, C. Huppa, *Craniomaxillofac. Trauma Reconstr.* **2016**, *9*, 1.
[10] A. C. Jayasuriya, A. Bhat, *J. Tissue Eng. Regener. Med.* **2010**, *4*, 340.
[11] A. Scarano, F. Lorusso, G. Staiti, B. Sinjari, A. Tampieri, C. Mortellaro, *Front. Physiol.* **2017**, *8*, 565.
[12] B. Gaihre, S. Uswatta, C. A. Jayasuriya, *J. Funct. Biomater.* **2017**, *8*, 49.
[13] Z. Sheikh, S. Najeeb, Z. Khurshid, V. Verma, H. Rashid, M. Glogauer, *Materials* **2015**, *8*, 9.
[14] D. P. Link, J. van den Dolder, J. G. C. Wolke, J. A. Jansen, *Tissue Eng.* **2007**, *13*, 493.
[15] F. Schwarz, A. Schmucker, J. Becker, *Clin. Oral Implants Res.* **2017**, *28*, 779.
[16] D. Gothard, E. L. Smith, J. M. Kanczler, C. R. Black, J. A. Wells, C. A. Roberts, L. J. White, O. Qutachi, H. Peto, H. Rashidi, M. M. Stevens, A. J. El-Haj, F. R. Rose, K. M. Shakesheff, R. O. Oreffo, *PLoS One* **2015**, *10*, e0145080.
[17] A. C. Mendes, K. H. Smith, E. Tejeda-Montes, E. Engel, R. L. Reis, H. S. Azevedo, A. Mata, *Adv. Funct. Mater.* **2013**, *23*, 430.
[18] S. Elsharkawy, M. Al-Jawad, M. F. Pantano, E. Tejeda-Montes, K. Mehta, H. Jamal, S. Agarwal, K. Shuturminska, A. Rice, N. V. Tarakina, R. M. Wilson, A. J. Bushby, M. Alonso, J. C. Rodriguez-Cabello, E. Barbieri, A. del Roi Hernández, M. M. Stevens, N. M. Pugno, P. Anderson, A. Mata, *Nat. Commun.* **2018**, *9*, 2145.
[19] E. Tejeda-Montes, A. Klymov, M. R. Nejadnik, M. Alonso, J. C. Rodriguez-Cabello, X. F. Walboomers, A. Mata, *Biomaterials* **2014**, *35*, 8339.
[20] S. Shimizu, S. Tsuchiya, A. Hirakawa, K. Kato, M. Ando, M. Mizuno, M. Osugi, K. Okabe, W. Katagiri, H. Hibi, *BMC Oral Health* **2019**, *19*, 69.
[21] P. A. Parmar, L. W. Chow, J.-P. St-Pierre, C.-M. Horejs, Y. Y. Peng, J. A. Werkmeister, J. A. M. Ramshaw, M. M. Stevens, *Biomaterials* **2015**, *54*, 213.
[22] H. Lopez Hernandez, A. K. Grosskopf, L. M. Stapleton, G. Agmon, E. A. Appel, *Macromol. Biosci.* **2019**, *19*, 1800275.
[23] J. H. Lee, M. Y. Ryu, H.-R. Baek, H.-K. Lee, J.-H. Seo, K. M. Lee, A. Y. Lee, G. B. Zheng, B.-S. Chang, C.-K. Lee, *Artif. Organs* **2014**, *38*, 149.
[24] E. Martínez-Sanz, O. P. Varghese, M. Kisiel, T. Engstrand, K. M. Reich, M. Bohner, K. B. Jonsson, T. Kohler, R. Müller, D. A. Ossipov, J. Hilborn, *J. Tissue Eng. Regener. Med.* **2012**, *6*, s15.
[25] W. Zhang, X. Wang, S. Wang, J. Zhao, L. Xu, C. Zhu, D. Zeng, J. Chen, Z. Zhang, D. Kaplan, X. Jiang, *Biomaterials* **2011**, *32*, 9415.
[26] T.-M. De Witte, L. E Fratila-Apachitei, A. A. Zadpoor, N. A , Peppas, *Regener. Biomater.* **2018**, *5*, 197.
[27] P. S. Lienemann, M. P. Lutolf, M. Ehrbar, *Adv. Drug Delivery Rev.* **2012**, *64*, 1078.
[28] J. D. Kretlow, S. Young, L. Klouda, M. Wong, A. G. Mikos, *Adv. Mater.* **2009**, *21*, 3368.
[29] B. O. Okesola, A. Mata, *Chem. Soc. Rev.* **2018**, *47*, 3721.
[30] B. O. Okesola, Y. Wu, B. Derkus, S. Gani, Y. Wu, D. Knani, D. K. Smith, D. J. Adams, A. Mata, *Chem. Mater.* **2019**, *31*, 7883.
[31] M. Liu, X. Zeng, C. Ma, H. Yi, Z. Ali, X. Mou, S. Li, Y. Deng, N. He, *Bone Res.* **2017**, *5*, 17014.
[32] P. Y. Shona, M. Kurisawa, S. Gao, J. E. Chung, J. Y. Ying, *Biomaterials* **2009**, *30*, 822.
[33] S. C. Dennis, J. Whitlow, M. S. Detamore, S. L. Kieweg, C. J. Berkland, *Langmuir* **2017**, *33*, 206.
[34] M. P. Hendricks, K. Sato, L. C. Palmer, S. I. Stupp, *Acc. Chem. Res.* **2017**, *50*, 2440.
[35] A. Mata, Y. Geng, K. J. Henrikson, C. Aparicio, S. R. Stock, R. L. Satcher, S. I. Stupp, *Biomaterials* **2010**, *31*, 6004.
[36] Z. Huang, T. D. Sargeant, J. F. Hulvat, A. Mata, P. Bringas Jr., C.-Y. Koh, S. I. Stupp, M. L. Snead, *J. Bone Miner. Res.* **2008**, *23*, 1995.
[37] R. N. Shah, N. A. Shah, M. M. Del Rosario Lim, C. Hsieh, G. Nuber, S. I. Stupp, *Proc. Natl. Acad. Sci. USA* **2010**, *107*, 3293.
[38] L. W. Chow, R. Bitton, M. J. Webber, D. Carvajal, K. R. Shull, A. K. Sharma, S. I. Stupp, *Biomaterials* **2011**, *32*, 1574.
[39] S. Unterman, L. F. Charles, S. E. Strecker, D. Kramarenko, D. Pivovarchik, E. R. Edelman, N. Artzi, *ACS Nano* **2017**, *11*, 2598.
[40] J. I. Dawson, R. O. C. Oreffo, *Adv. Mater.* **2013**, *25*, 4069.
[41] M. Mousa, N. D. Evans, R. O. C. Oreffo, J. I. Dawson, *Biomaterials* **2018**, *159*, 204.
[42] A. K. Gaharwar, L. M. Cross, C. W. Peak, K. Gold, J. K. Carrow, A. Brokesh, K. A. Singh, *Adv. Mater.* **2019**, *31*, 1900332.
[43] S. Basu, S. Pacelli, Y. Feng, Q. Lu, J. Wang, A. Paul, *ACS Nano* **2018**, *12*, 9866.
[44] L. Tao, L. Zhonglong, X. Ming, Y. Zezheng, L. Zhiyuan, Z. Xiaojun, W. Jinwu, *RSC Adv.* **2017**, *7*, 54100.
[45] D. Su, L. Jiang, X. Chen, J. Dong, Z. Shao, *ACS Appl. Mater. Interfaces* **2016**, *8*, 9619.
[46] J. R. Xavier, T. Thakur, P. Desai, M. K. Jaiswal, N. Sears, E. Cosgriff-Hernandez, R. Kaunas, A. K. Gaharwar, *ACS Nano* **2015**, *9*, 3109.

[47] C. Loebel, M. D'Este, M. Alini, M. Zenobi-Wong, D. Eglin, *Carbohydr. Polym.* **2015**, *115*, 325.
[48] L. Pickart, A. Margolina, *Int. J. Mol. Sci.* **2018**, *19*, 1987.
[49] A. Darr, A. Calabro, *J. Mater. Sci.: Mater. Med.* **2009**, *20*, 33.
[50] C. Loebel, S. E. Szczesny, B. D. Cosgrove, M. Alini, M. Zenobi-Wong, R. L. Mauck, D. Eglin, *Biomacromolecules* **2017**, *18*, 855.
[51] J. Lee, M. Ju, O. H. Cho, Y. Kim, K. T. Nam, *Adv. Sci.* **2019**, *6*, 1801255.
[52] K. Xu, K. Narayanan, F. Lee, K. H. Bae, S. Gao, M. Kurisawa, *Acta Biomater.* **2015**, *24*, 159.
[53] Y. Liu, H. Meng, S. Konst, R. Sarmiento, R. Rajachar, B. P. Lee, *ACS Appl. Mater. Interfaces* **2014**, *6*, 16982.
[54] A. J. Engler, S. Sen, H. L. Sweeney, D. E. Discher, *Cell* **2006**, *126*, 677.
[55] O. Chaudhuri, L. Gu, D. Klumpers, M. Darnell, S. A. Bencherif, J. C. Weaver, N. Huebsch, H.-P. Lee, E. Lippens, G. N. Duda, D. J. Mooney, *Nat. Mater.* **2016**, *15*, 326.
[56] V. B. Bueno, R. Bentini, L. H. Catalani, D. F. S. Petri, *Carbohydr. Polym.* **2013**, *92*, 1091.
[57] S. K. Hahn, J. K. Park, T. Tomimatsu, T. Shimoboji, *Int. J. Biol. Macromol.* **2007**, *40*, 374.
[58] H.-Y. Lee, C.-H. Hwang, H.-E. Kim, S.-H. Jeong, *Carbohydr. Polym.* **2018**, *186*, 290.
[59] J. A. Burdick, G. D. Prestwich, *Adv. Mater.* **2011**, *23*, H41.
[60] S. Sharifi, S. B. G. Blanquer, T. G. van Kooten, D. W. Grijpma, *Acta Biomater.* **2012**, *8*, 4233.
[61] M. E. Klontzas, S. Reakasame, R. Silva, J. C. F. Morais, S. Vernardis, R. J. MacFarlane, M. Heliotis, E. Tsiridis, N. Panoskaltsis, A. R. Boccaccini, A. Mantalaris, *Acta Biomater.* **2019**, *88*, 224.
[62] H. Yukawa, K. Suzuki, K. Aoki, T. Arimoto, T. Yasui, N. Kaji, T. Ishikawa, T. Ochiya, Y. Baba, *Sci. Rep.* **2018**, *8*, 6765.
[63] S. Jose, M. L. Hughbanks, B. Y. K. Binder, G. C. Ingavle, J. K. Leach, *Acta Biomater.* **2014**, *10*, 1955.
[64] J. Pauty, R. Usuba, I. G. Cheng, L. Hespel, H. Takahashi, K. Kato, M. Kobayashi, H. Nakajima, E. Lee, F. Yger, F. Soncin, Y. T. Matsunaga, *EBioMedicine* **2018**, *27*, 225.
[65] X. Wang, B. Liu, Q. Xu, H. Sun, M. Shi, D. Wang, M. Guo, J. Yu, C. Zhao, B. Feng, *Wound Repair Regener.* **2017**, *25*, 270.
[66] M. D. Bresaola, M. A. Matsumoto, A. Zahoui, C. C. Biguetti, H. Nary-Filho, *Clin. Oral Implants Res.* **2017**, *28*, 320.
[67] N. R. Raia, B. P. Partlow, M. McGill, E. P. Kimmerling, C. E. Ghezzi, D. L. Kaplan, *Biomaterials* **2017**, *131*, 58.
[68] A. Mata, L. Palmer, E. Tejeda-Montes, S. I. Stupp, *Methods Mol. Biol.* **2012**, *811*, 39.

ADVANCED FUNCTIONAL MATERIALS

Editorial Office:
Wiley-VCH Verlag
Boschstraße 12, 69469 Weinheim
Germany
Tel.: (+49) 6201 606 531
Fax: (+49) 6201 606 510

Email: afm@wiley-vch.de

Reprint Order Form

Manuscript No.: _____
Customer No.: (if available) _____
Purchase Order No.: _____
Author: _____

Charges for Reprints in Euro (excl. VAT), prices are subject to change. Minimum order 50 copies; single issues for authors at a reduced price.

No. of pages	50 copies	100 copies	150 copies	200 copies	300 copies	500 copies
1– 4	345,—	395,—	425,—	445,—	548,—	752,—
5– 8	490,—	573,—	608,—	636,—	784,—	1077,—
9–12	640,—	739,—	786,—	824,—	1016,—	1396,—
13–16	780,—	900,—	958,—	1004,—	1237,—	1701,—
17–20	930,—	1070,—	1138,—	1196,—	1489,—	2022,—
every additional 4 pages	147,—	169,—	175,—	188,—	231,—	315,—

Information regarding VAT: The charges for publication of *cover pictures /reprints/issues/poster/Video abstracts/* are considered to be "supply of services" and therefore subject to German VAT. However, if you are an institutional customer outside Germany, the tax can be waived if you provide us with the valid VAT number of your company. Non-EU customers may have a VAT number starting with "EU" instead of their country code, if they are registered with the EU tax authorities. If you do not have a valid EU VAT number and you are a taxable person doing business in a non-EU country, please provide a certification from your local tax authorities confirming that you are a taxable person under local tax law. Please note that the certification must confirm that you are a taxable person and are conducting an economic activity in your country. **Note:** certifications confirming that you are a tax-exempt legal body (non-profit organization, public body, school, political party, etc.) in your country do not exempt you from paying German VAT.

Please send me send bill me for

☐ no. of reprints

☐ no. of issue
(1 copy: 28 Euro)

☐ high-resolution PDF file (330 Euro excl. VAT)
E-mail address: _____

❖ Special Offer:
If you order 200 or more reprints you will get a PDF file for half price.

Please note: It is not permitted to present the PDF file on the internet or on company homepages.

Cover Posters (prices excl. VAT)
Posters of published covers are available in two sizes:

☐ DIN A2 42 x 60 cm / 17 x 24in (one copy: 39 Euro)

☐ DIN A1 60 x 84 cm / 24 x 33in (one copy: 49 Euro)

Postage for shipping (prices excl. VAT)
overseas +25 Euro
within Europe +15 Euro

_____
Date, Signature

VAT number: _____

Mail reprints / copies of the issue to:

_____
_____
_____
_____
_____

Send bill to:

_____
_____
_____
_____

☐ **I will pay by bank transfer**

☐ **I will pay by credit card**

VISA, Mastercard and AMERICAN EXPRESS
For your security please use this link (Credit Card Token Generator) to create a secure code Credit Card Token and include this number in the form instead of the credit card data. Click here:
https://www.wiley-vch.de/editorial_production/index.php

CREDIT CARD TOKEN NUMBER

						V									

Wiley-VCH Verlag GmbH & Co. KGaA – A company of John Wiley & Sons, Inc. -
Location of the Company: Weinheim - Trade Register: Mannheim, HRB 432833.
Chairman of the Supervisory Board: John Kritzmacher
General Partner: John Wiley & Sons GmbH, Location: Weinheim –
Trade Register Mannheim, HRB 432296 – Managing Director: Sabine Haag and Dr. Guido Herrmann

WILEY-VCH